RESEARCH ARTICLE | JANUARY 08 2026

Supercritical water at ten densities from 0.1 to 1.0 gr/cc at 1000 K using *ab initio* molecular dynamics simulations

Nitish Baradwaj ; Ken-ichi Nomura ; Aiichiro Nakano ; Rajiv K. Kalia ; Priya Vashishta

J. Chem. Phys. 164, 024501 (2026)
https://doi.org/10.1063/5.0303702

The Journal of Chemical Physics ARTICLE pubs.aip.org/aip/jcp

Supercritical water at ten densities from 0.1 to 1.0 gr/cc at 1000 K using *ab initio* molecular dynamics simulations

Cite as: J. Chem. Phys. 164, 024501 (2026); doi: 10.1063/5.0303702
Submitted: 23 September 2025 • Accepted: 18 December 2025 •
Published Online: 8 January 2026

Nitish Baradwaj, Ken-ichi Nomura, Aiichiro Nakano, Rajiv K. Kalia, and Priya Vashishta[a]

AFFILIATIONS

Collaboratory for Advanced Computing and Simulations, Department of Chemical Engineering and Materials Science, Department of Computer Science, and Department of Physics & Astronomy, University of Southern California, Los Angeles, California 90089-0242, USA

[a]Author to whom correspondence should be addressed: priyav@usc.edu

ABSTRACT

Supercritical water is found inside Earth's mantle, where water is subjected to very high temperatures and pressures. It exhibits extraordinary properties, such as having a low dielectric constant and high reactivity, which stems from the breakdown of the hydrogen bond network in a supercritical state. This makes supercritical water a non-polar solvent and the basis for many innovative technologies. We investigate supercritical water at ten densities (0.1–1.0 gr/cc) at 1000 K to study the structural correlations, such as atom-resolved partial pair distributions, co-ordination numbers, bond-angle distributions and neutron scattering, and x-ray structure factors. Among the dynamical correlations, we investigate the velocity autocorrelation function, current–current correlation function, and their Fourier transforms—vibrational density-of-states and frequency dependent dielectric constant. Structural and dynamical correlations are computed from time-trajectories of the positions and velocities calculated *ab initio* molecular dynamics within the density functional theory framework using the SCAN exchange–correlation functional. Our results for structural correlations are compared with the neutron scattering experiments on supercritical water by Soper and collaborators [J. Chem. Phys. **106**, 247–254 (1997)] and dynamical correlations in the supercritical state are compared with the inelastic neutron scattering results by Car and collaborators [J. Phys. Chem. Lett. **11**, 9461–9467 (2020)].

I. INTRODUCTION

Water on the Earth is an essential component of life at ambient temperatures and pressure. Life as we know it would not exist without water. Scientists are looking for signatures of water/water vapor in exoplanets as the first sign of life. 71% of our planet's surface is water,[1] giving its iconic blue color. Most of the surface water is in the Oceans (about 96.5%). However, this is only a fraction compared to what is stored in Earth's interior. Water exists in Earth's mantle in a supercritical state[2] (647 K, 221 MPa). Supercritical water (SCW) in the mantle plays an important role in regulating the global water cycle by circulating surface water deep into the mantle and back up to the surface again.[3] This process enriches the surface of the Earth in minerals and salts. Water in its supercritical state is a very strong solvent.[4] The high diffusivity of SCW enables it to penetrate voids and fissures. Most silicates and carbonates are practically insoluble in water at ambient temperatures and pressure. However, the solubility of these minerals increases tenfold under supercritical conditions. Silicates and carbonates present on the Earth's surface owe their presence due to this cycle.[3,5] SCW is responsible for volcanism in subduction zones in the Earth. The olivines $(Mg/Fe)_2SiO_4$ in the Earth's mantle are transformed into serpentine minerals $(Mg/Fe)_3Si_2O_5(OH)_4$ with the uptake of the OH group. This oxidation of Fe^{+2} to Fe^{+3} leads to the formation of magnetite and the production of hydrogen gas. It has been theorized that this is one of the main mechanisms of hydrogen producing processes on Earth. A research study by Hovland *et al.*[6,7] have shown that the large deposits of salt in the Red Sea can be attributed to SCW in hydrothermal systems deep in the Earth's mantle. The marine life around these brine pools may be where life first started on our

planet. Studying the micro-organisms adapted to such harsh conditions can help us in understanding the formation and evolution of life not just on our planet but in various exo-planets as well.

The properties of SCW are very different when compared to that of ambient water. The dielectric constant of SCW drops from a value of 80 for ambient water to around 2 for SCW.[8] The ionic disassociation constant drops from 10^{-14} to 10^{-23} in SCW. This makes SCW completely miscible with non-polar fluids. One interesting application of SCW, which results from its non-polar nature, is its ability to transport petroleum. Petroleum can be dissolved in SCW and transported from oil rigs to refineries where the steam can be condensed and the oil precipitates out. This property of SCW is also useful in "green" carbon capture technologies where hazardous organic compounds are catalytically oxidized to form other environmentally harmless products. SCW thus falls into the "green solvent[9]" category. SCW is also completely miscible with oxygen, thereby creating the perfect conditions for oxidation of organics.[10] The process known as supercritical water oxidation (SCWO) is defined as continuous oxidation of chemicals in SCW using oxygen or hydrogen peroxide as oxidizing agents. Environmentally efficient and carbon friendly, SCWO completely eliminates all the oxidizable material.[11] SCWO has been shown to be effective in eliminating effects of chemical weapons.[12] One of the main advantages of supercritical water as a solvent is that organic compounds are brought into molecular contact in a homogenous phase. The oxidation process is not limited by transportation because of the high temperature involved. Furthermore, this makes the kinetics fast and the reaction proceeds to completion rapidly.

We need to understand the properties of SCW to improve the scalability and sustainability of highly reactive oxidation processes. The properties of SCW stem from its inherent structure, and therefore, it becomes essential to understand structural and correlations in SCW. The structural correlations in SCW still remain elusive. In particular, the degree and nature of hydrogen bonds in SCW have been topics of discussion in the community. The article by Sahle *et al.*[13] highlighted the need for simulation and experiments required to understand the structure of SCW. Several studies exist that examine the structure of SCW[13–16] but these simulation studies involve classical MD forcefields that are not entirely reliable under supercritical conditions of temperature and pressure or other scattering experiments where dynamics of the system is not fully considered. In our study, we investigate both the structure and dynamics of SCW calculated from DFT-based quantum simulations over ten densities ranging from 0.1 to 1.0 g/cc at a temperature of 1000 K. One other challenge in demystifying the structure of SCW is the temperature at which experiments must be carried out. The results of these experiments,[17,18] therefore, do not provide a consensus in establishing the structure of SCW. Using neutron scattering data, Postorino *et al.*[19] concluded that SCW contained a broken hydrogen bond network with high disorder. However, optical Raman spectra studies[20–22] conclude that majority of the hydrogen bond network remains intact through the supercritical phase. Sun *et al.*[14] carried out Raman spectra studies in SCW and concluded that the hydrogen bonding is closely related to pressure and temperature. Their study revealed that closer to the critical point, the tetrahedral hydrogen bonding disappears and chain-like hydrogen bonding structure emerges. This result was further supported with NMR studies carried out by Hoffman and Conradi[23] X-ray Raman spectroscopic studies by Wernet *et al.*[15] concluded that SCW consisted of small dense clusters of hydrogen bonded regions surrounded by less dense regions. Studies have shown that interpreting small angle scattering data might not be straightforward.[13,24,25]

Ab initio quantum simulations based on DFT provide an accurate description of quantum mechanically interatomic forces that include electron–electron and electron–ion interactions when compared to an empirically fitted molecular dynamics under at ambient conditions of temperature and pressure. Quantum simulations enable us to not only extract the accurate atomic level structure but also the vibrational density-of-states and IR spectra,[13,26,27] which can be calculated by Fourier transforming velocity autocorrelation functions and the current–current autocorrelations, respectively. Electronic ground state modeling of the water system is accurate with DFT; however, we must turn to exchange–correlation functionals (XC) to describe the many body effects in the system. Perdew and Schmidt[28] have arranged various XC functionals according to Jacob's ladder, with the LDA[29] on the lower end and *meta*-GGAs and hybrid functionals[30] on the other side. In an article, Car[31] talks about how SCAN moves the *meta*-GGA rung much closer to the fourth rung of hybrid functionals. The density of water at 330 K produced from SCAN is 1.050 ± 0.027 and that of Ice Ih at 273 K is 0.964 ± 0.023, which leads to ice floating on water. PBE functionals predict the density of water (330 K) and ice (273 K) as 0.850 ± 0.016 and 0.936 ± 0.013, respectively, which leads to ice sinking in water. This difference in density can be attributed to the increased packing resulting from the inclusion of intermediate non-directional vdW interactions in SCAN. There is also an overestimation of hydrogen bond strength by SCAN stemming from the self-interaction errors. However, this is a limitation with most XCs and not just SCAN.

There are limitations with the SCAN with the non-inclusion of long-range vdW interactions, which are significant in bulk water phases as opposed to small water clusters. This, however, would result in SCAN not being able to describe experimental Ice Ih structures.[32] These limitations of SCAN must always be kept in mind while analyzing the results of DFT-based calculations of water under ambient conditions as well as in supercritical states.

II. METHOD

We used Vienna Ab initio Simulation Package (VASP) software[33] to perform quantum molecular dynamics (QMD) simulations.[34] The electronic states are calculated using the projector augmented-wave (PAW) method[35] in the framework of density functional theory (DFT).[36] The exchange–correlation effects are incorporated using the SCAN functional.[37]

We start simulations with a bulk water configuration taken from our previous study of water,[38] which contains 108 H_2O molecules. We have simulated a system of 108 water molecule (324 atoms) system at a density of 1 g/cc at 1000 K. After thermalizing these systems in the NVT ensemble for 2000 steps, we decreased the density of the system in steps of 0.1 g/cc, followed by thermalization for 2000 steps. This process was repeated until we had ten thermalized systems with various densities 0.1–1.0 g/cc at a temperature of 1000 K. Starting from these thermalized systems, we ran 40 000 steps in the NVE ensemble with a time step of 0.25 fs (a total of 400 000 steps for ten densities) to calculate the structural and dynamical correlations of SCW.

III. STRUCTURAL CORRELATIONS $g_{\alpha\beta}(r)$, $g(r)$, $g_N(r)$, $S_{\alpha\beta}(q)$, $S(q)$, $S_N(q)$, and $S_X(q)$ AND VALIDATION WITH NEUTRON SCATTERING EXPERIMENTS FOR SCW AT 0.75 gr/cc AT 673 K

A. Structural properties

For the ten systems, from their MD trajectories, we have computed partial pair distribution functions, $g_{\alpha\beta}(r)$, and the neutron pair distribution function, $g_N(r)$.[39] The neutron pair distribution function is defined as

$$g_N(r) = \frac{\sum_{\alpha,\beta} c_\alpha b_\alpha c_\beta b_\beta g_{\alpha\beta}(r)}{\left(\sum_\alpha b_\alpha c_\alpha\right)^2}, \quad (1)$$

where r is the pair distance and c_α and b_α are the concentration and coherent neutron-scattering length of species α, respectively.

To provide more complete structural correlation results for the recent and future scattering experiments, we have computed partial static structure factors, $S_{\alpha\beta}$ (q), from the Fourier transform of corresponding partial pair distribution functions,[39]

$$S_{\alpha\beta}(q) = \delta_{\alpha\beta} + 4\pi\rho\left(c_\alpha c_\beta\right)^{1/2} \int_0^\infty \left[g_{\alpha\beta}(r) - 1\right] \frac{\sin(qr)}{qr} r^2 dr, \quad (2)$$

where q is the wave number, ρ is the total number density, and c_α is the concentration of species α.

The neutron-scattering static structure, $S_N(q)$, is obtained from the partial static structure factors by weighting them with concentration and coherent neutron-scattering lengths,[39]

$$S_N(q) = \frac{\sum_{\alpha,\beta} b_\alpha b_\beta \left(c_\alpha c_\beta\right)^{1/2} S_{\alpha\beta}(q)\left[S_{\alpha\beta}(q) - \delta_{\alpha\beta} + \left(c_\alpha c_\beta\right)^{1/2}\right]}{\left(\sum_\alpha b_\alpha c_\alpha\right)^2}, \quad (3)$$

where b_α is the coherent neutron-scattering length of species α.

The x-ray structure factor, $S_X(q)$, is obtained by[39]

$$S_X(q) = \frac{\sum_{\alpha,\beta} f_\alpha f_\beta \left(c_\alpha c_\beta\right)^{1/2} S_{\alpha\beta}(q)}{\left(\sum_\alpha f_\alpha c_\alpha\right)^2}, \quad (4)$$

where f_α is the x-ray from the factor of species α.

B. Validation of structural correlations obtained from simulations with neutron scattering experiments for SCW at 0.75 gr/cc at 673 K

To validate our quantum dynamics simulation results, we first compare calculated structural properties with neutron scattering experiment on supercritical water by Bernabei, Soper *et al.*[40,41] These authors have determined the pair distribution functions of supercritical water at a density of 0.75 gr/cc at 673 K. Before we report our predictions for structural correlations for densities 0.1–1.0 gr/cc, it is useful to validate the accuracy of our DFT-SCAN-based simulation with available experimental data. Quality of agreement and any discrepancies will be a useful guide for further discussions.

To validate our QMD simulations, we first examine the neutron pair distribution function, $g_N(r)$, computed from QMD simulations with neutron scattering experiments for SCW at 673 K, with a density of 0.75 g/cc. This is the most direct comparison with the neutron experiment because it only requires Fourier transform of the observed neutron structure factor from experiment.[40] The results for neutron pair distribution function, $g_N(r)$, along with experimental results are plotted in Fig. 1(e). For easy reference, we have also plotted all the structural properties of water under ambient conditions (300 K, 1.0 g/cc) by the dashed black lines. The experimental neutron results, wherever available, from Bernabei *et al.*[40] are plotted as the dotted blue lines. It is clear that there is good agreement between the neutron experiment (blue) and QMD results (red). In addition, the partial pair distributions, $g_{\alpha\beta}(r)$, for O–O, O–H, and H–H are shown along with experimentally derived $g_{\alpha\beta}(r)$ in Figs. 1(a)–1(c). The agreement between experimentally derived $g_{\alpha\beta}(r)$ and our QMD results is good for O–O and O–H. There are large deviations for H–H between experiment and QMD results. We would like to point out that the experimentally derived results for H–H are the least reliable because of the opposite signs of H and D neutron cross sections. We stand by our QMD results for $g_{\alpha\beta}(r)$ to be accurate and more reliable for H–H than the experimentally derived values.

Bond angles computed from QMD simulations of water at 673 K with density of 0.75 g/cc are plotted in red in the middle column along with the computed ones for water under ambient conditions indicated by dashed black. We indicate by the single dash the covalent bond and the hydrogen bond by the two dashes. The double covalent H–O–H bond angle is shown in Fig. 1(f). When compared to ambient water, the peak of the bond distribution for supercritical water remains unchanged; however, the distribution skews toward lower angles. Figure 1(g) shows the H–O–H bond angle between the H–O hydrogen bond and the O–H covalent bond, which shows a shift in the position of the peak as well as skewing toward lower angles. Similar features are seen in Fig. 1(h) that shows the double hydrogen bond angle H–O–H. Figure 1(i) shows the O–H–O bond angle between the covalent O–H bond and H–O hydrogen bond, where the structure in the bond angle distribution becomes quite flat. The intermolecular OOO bond angle distribution is shown in Fig. 1(j) in the middle column, which also becomes quite flat. Partial structure factors, $S_{\alpha\beta}(q)$, computed from QMD simulations are shown in the right column of Figs. 1(k)–1(m) (in red) along with the computed partials for ambient water indicated by the black dashed lines. The x-ray structure factor $S_X(q)$ and the neutron structure factor $S_N(q)$ are also plotted in Figs. 1(n) and 1(o), respectively. The results for partial pair distribution functions and neutron weighted pair distribution function from QMD for ambient water are shown in Fig. 2.

C. Structural correlation results

Having validated our QMD simulation results with the neutron experimental data for water at 673 K with a density of 0.75 g/cc, we now present structural and vibrational properties for supercritical water. We have performed QMD simulations over a range of densities (0.1–1.0 g/cc) at 1000 K. In this section, we will present results for densities 1.0, 0.8, 0.5, 0.3, and 0.1 g/cc at 1000 K. The results for other densities 0.9, 0.7, 0.6, 0.4, and 0.2 are given in the supplementary material.

Our simulation results for partial pair distribution function, $g_{\alpha\beta}(r)$, at the density of 1 g/cc are plotted in the left column of Figs. 3(a)–3(c) (in red) along with their values for ambient water (in black dashed lines). The total pair distribution function, $g(r)$, and neutron weighted pair distribution function, $g_N(r)$, are also

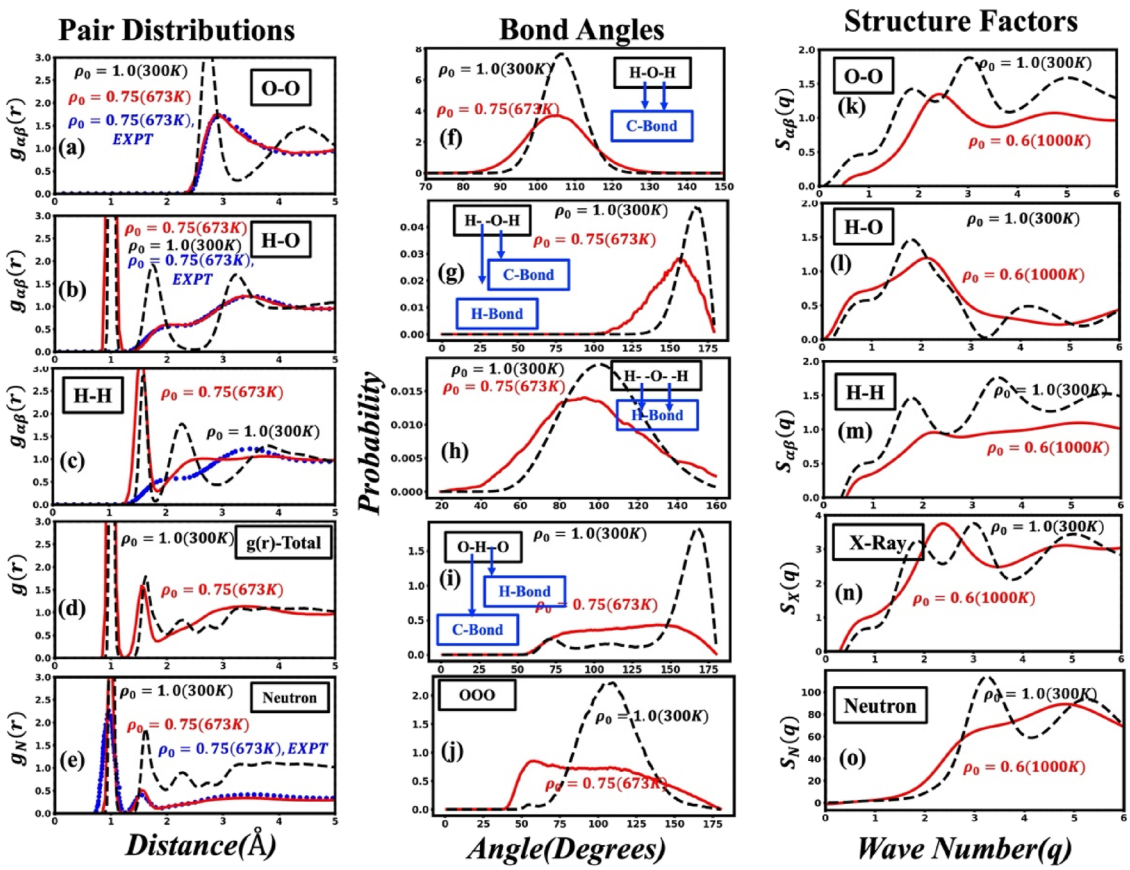

FIG. 1. Validation of structural correlations with neutron scattering experiments. Neutron pair distribution function, $g_N(r)$, computed from QMD simulations is compared with neutron scattering experiments for SCW at 673 K, with a density of 0.75 g/cc. We emphasize that the temperature and density are identical for the QMD simulations and the neutron scattering experiment. The results for our QMD simulations are plotted in red. For easy reference, we have also plotted all the structural properties of water under ambient conditions (300 K, 1.0 g/cc) by the black dashed lines. The experimental neutron results, wherever available, from Bernabei *et al.*[40] [Reproduced with permission from Bernabei *et al.*, Phys. Rev. E **78**, 021505 (2008). Copyright 2008, American Physical Society] are plotted by the blue dotted lines. The three columns from left to right are pair distribution functions, bond angles distributions, and structure factors. The first column compares the QMD, $g_{\alpha\beta}(r)$, figures (a)–(c) (red) with the neutron experiment (dotted blue). The black dashed curves represent ambient water for reference, to contrast the changes in the SCW state. The total $g(r)$ and $g_N(r)$ are plotted in panels (d) and (e), respectively. Experimental data for $g_N(r)$ are obtained directly from neutron measurement that are considered most reliable. It should be noted that partials, $g_{\alpha\beta}(r)$, derived from various subtractions by neutron scientists are less reliable, when compared to $g_N(r)$. In the first column of panel (e), our QMD, $g_N(r)$, (in red) agrees well with the experimental values (blue dotted line). It is indeed very gratifying to see this agreement. We also compare $g_{\alpha\beta}(r)$, for O–O, O–H, and H–H. The agreement between experimentally derived $g_{\alpha\beta}(r)$ and our QMD results is good for O–O and O–H. There are large deviations for H–H between the experiment and QMD results. It should be emphasized that the experimentally derived results for H–H are the least reliable because of opposite signs of H and D neutron cross sections. We stand by our QMD results to be accurate and more reliable for H–H. Computed bond angles of water at 673 K with density of 0.75 g/cc are plotted in red in the middle column along with the ones computed for water under ambient conditions represented by the black dashed lines. The double covalent H–O–H bond angle is in panel (f). Panel (g) shows the H–O–H bond angle between the H–O hydrogen bond and the O–H covalent bond. The single dash indicates covalent bond, and the two dashes indicate the hydrogen bond. Panel (h) shows the double hydrogen bond angle H–O–H. Panel (i) shows the O–H–O bond angle between the covalent O–H bond and the hydrogen H–O bond, and panel (j) in the middle column shows the intermolecular OOO bond angle. Computed partial structure factors, $S_{\alpha\beta}(q)$, are plotted on the right column of panels (k)–(m) (in red) along with the computed partials indicated by the black dashed lines. The x-ray structure factor $S_X(q)$ and the neutron structure factor, $S_N(q)$, are also plotted in panels (n) and (o), respectively.

plotted in Figs. 3(d) and 3(e), respectively. Computed bond angles of water at 1000 K with the density of 1.0 g/cc are plotted in red in the middle column along with the ones computed for water under ambient conditions plotted by the black dashed lines. The double covalent H–O–H bond angle is shown in Fig. 3(f). Figure 3(g) shows the H–O–H bond angle between the H–O hydrogen bond and the O–H covalent bond. The single dash indicates covalent bond, and two dashes indicate the hydrogen bond. Figure 3(h) shows the double hydrogen bond angle H–O–H. Figure 3(i) shows the O–H–O bond angle between the covalent O–H bond and the hydrogen H–O bond, and the middle column of Fig. 3(j) shows the intermolecular OOO bond angle. Computed partial structure factors, $S_{\alpha\beta}(q)$, are plotted on the right column, Figs. 3(k)–3(m) (in red) along with the computed partials plotted by the black dashed lines. The x-ray

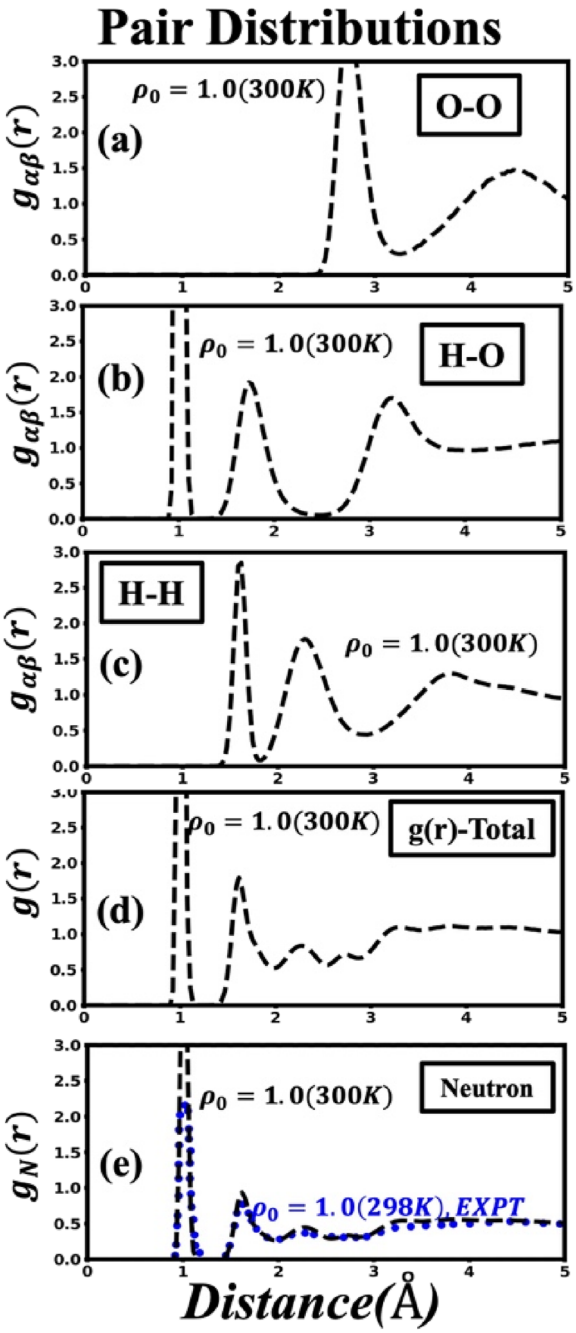

FIG. 2. Calculated structural properties of water at ambient temperature and pressure (300 K, 1.0 g/cc) are represented by the black dashed lines. We have also plotted the experimental results from Soper *et al.*[42] [Reproduced with permission from Soper *et al.*, Int. Scholarly Res. Not. **2013**(1), 1 (2013). Copyright 2013 Authors, licensed under a Creative Commons Attribution (CC BY) license.] by the blue dotted line. Computed partial pair distribution function, $g_{\alpha\beta}(r)$, is plotted in panels (a)–(c). The total pair distribution function, $g(r)$, and neutron weighted pair distribution function $g_N(r)$ are also plotted in panels (d) and (e), respectively. The experimentally obtained[42] $g_N(r)$ value is plotted for reference. Our computed value (black dashed lines) agrees well with the neutron experiment (blue dotted line).

structure factor, $S_X(q)$, and the neutron structure factor, $S_N(q)$, are also plotted in Figs. 3(n) and 3(o), respectively.

There are two variables that affect the structure of supercritical water: (1) The effect of temperature. This is examined when temperature is increased from 300 to 1000 K while maintaining density at 1.0 g/cc. (2) The effect of density is examined by changing the density from 1.0 to 0.1 g/cc while keeping the temperature constant at 1000 K.

First, we will discuss the effect of temperature at a density of 1.0 g/cc. At the density of 1.0 g/cc, we evaluate the integrity of the water molecule by examining $g_{\mathrm{HO}}(r)$, as shown in Fig. 3(b). The first peak in $g_{\mathrm{HO}}(r)$ appears at 1.02 Å, close to the ambient water O–H bond length of 0.98 Å, indicating that the covalent bond remains robust even at 1000 K. The first peak in $g_{\mathrm{HH}}(r)$, shown in Fig. 3(c), remains sharply defined at 1.62 Å, further confirming the intramolecular geometry of the water molecule. This fact is further confirmed by the bond angle distribution plots. The intramolecular H–O–H angle distribution in Fig. 3(f) shows a peak at 103° at 1000 K, slightly shifted from the 104° for room temperature water, further confirming the geometry of the water molecule. Next, we examine the hydrogen-bond network, as manifested in the second peak of $g_{\mathrm{HO}}(r)$ that becomes significantly weakened and the second and third peak merge at 1000 K. In Fig. 3(a), we compare the O–O radial distribution function $g_{\mathrm{OO}}(r)$ for water at 300 and 1000 K. At 300 K, the first O–O peak occurs at 2.73 Å, whereas at 1000 K, it moves to 2.85 Å. The identity of the second peak is well-defined at room temperature water is lost at 1000 K. At a temperature of 1000 K, there is a broadening of the intramolecular H–O–H bond angle, which stems from the thermal effect. The H–O–H bond angle shown in Fig. 3(g) peaks at 165° for ambient water and for water at 1000 K, this value peaks at 150° and broadens toward the lower angles. The hydrogen bond angle distribution H–O–H in Fig. 3(h) also shows a well-defined peak at 101°, with only moderate broadening, in contrast to the wide and flattened distribution spanning at 1000 K. Both the x-ray and neutron structure factors in Figs. 3(n) and 3(o) show more structure for room temperature water compared to water at 1000 K.

Partial pair distribution functions computed from QMD simulations, $g_{\alpha\beta}(r)$, at the density of 0.8 g/cc are plotted in the left columns of Figs. 4(a)–4(c) (by the red lines) along with their values for ambient water (by the black dashed lines). The total pair distribution function, $g(r)$, and neutron weighted pair distribution function, $g_N(r)$, are also plotted in Figs. 4(d) and 4(e), respectively. Computed bond angles of water at 1000 K with density of 1.0 g/cc are plotted by red in the middle column along with the ones computed for water under ambient conditions plotted by the black dashed lines. The double covalent H–O–H bond angle is shown in Fig. 4(f). Figure 4(g) shows the H–O–H bond angle between the H–O hydrogen bond and the O–H covalent bond. The single dash indicates covalent bond, and two dashes indicate the hydrogen bond. Figure 4(h) shows the double hydrogen bond angle H–O–H. Figure 4(i) shows the O–H–O bond angle between the covalent O–H bond and the hydrogen H–O bond, and the middle column of Fig. 4(j) shows the intermolecular OOO bond angle. Computed partial structure factors, $S_{\alpha\beta}(q)$, are plotted in the right columns of Figs. 4(k)–4(m) (in red) along with the computed partials plotted by the black dashed lines. The x-ray structure factor, $S_X(q)$, and the neutron structure factor, $S_N(q)$, are also plotted in Figs. 4(n) and 4(o), respectively.

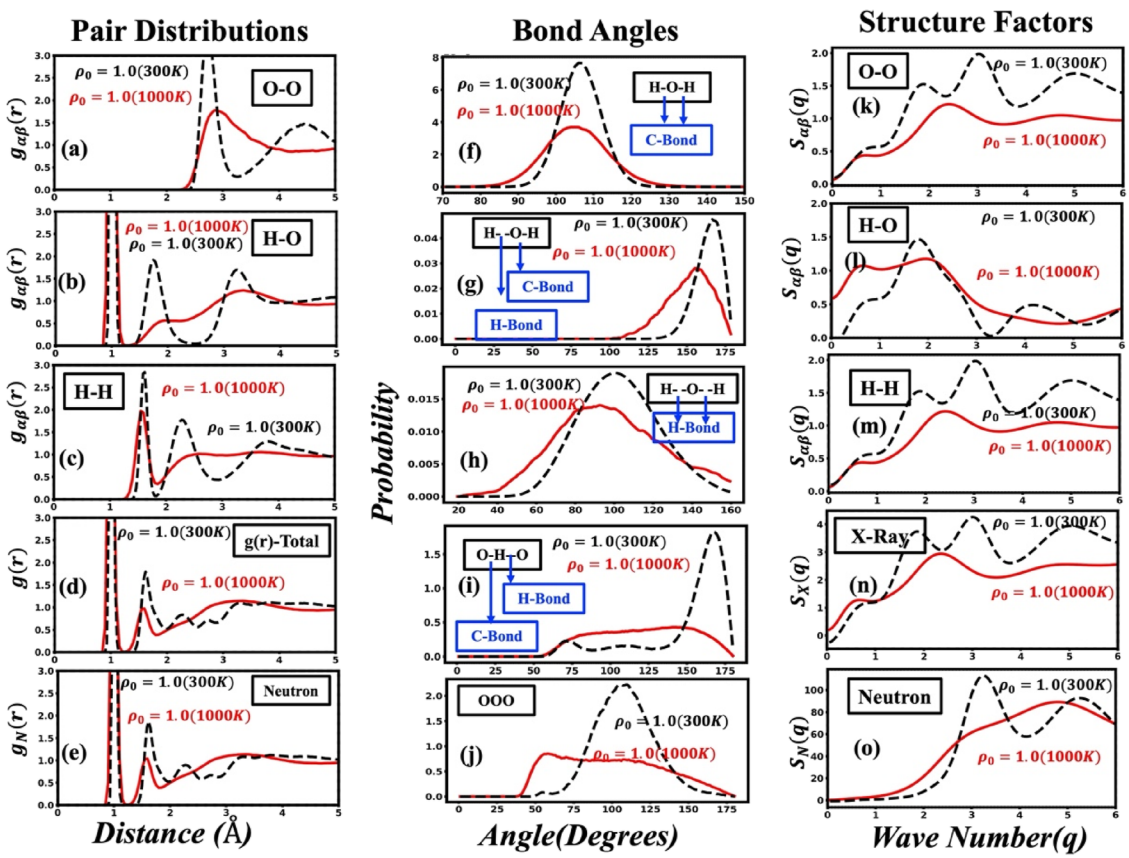

FIG. 3. Calculated structural properties of water at 1000 K, with a density of 1.0 g/cc from our QMD simulations are plotted in red. The structural properties of water at ambient temperature and pressure (300 K, 1.0 g/cc) are also plotted by the black dashed lines. The columns from left to right are calculated pair distribution functions, bond angles, and various structure factors, respectively.

Structural correlations that include partial pair distribution function $g_{\alpha\beta}(\mathrm{r})$ at a density of 0.5 g/cc are plotted on the left column of Figs. 5(a)–5(c) (red lines) along with their values for ambient water (black dashed lines). The total pair distribution function, $g(\mathrm{r})$, and neutron weighted pair distribution function, $g_N(\mathrm{r})$, are also plotted in Figs. 5(d) and 5(e), respectively. Computed bond angles of water at 1000 K with density of 1.0 g/cc are plotted in red in the middle column along with the ones computed for water under ambient conditions plotted by the black dashed lines. The double covalent H–O–H bond angle is shown in Fig. 5(f). Figure 5(g) shows the H–O–H bond angle between the H–O hydrogen bond and the O–H covalent bond. The single dash indicates covalent bond, and two dashes indicate the hydrogen bond. Figure 5(h) shows the double hydrogen bond angle H–O–H. Figure 5(i) shows the O–H–O bond angle between the covalent O–H bond and the hydrogen H–O bond and the middle column of Fig. 5(j) shows the intermolecular OOO bond angle. Computed partial structure factors, $S_{\alpha\beta}(q)$, are plotted in the right column of Figs. 5(k)–5(m) (in red) along with the computed partials plotted by the black dashed lines. The x-ray structure factor, $S_X(q)$, and the neutron structure factor, $S_N(q)$, are also plotted in Figs. 5(n) and 5(o), respectively.

We have computed partial pair distribution function $g_{\alpha\beta}(r)$ at a density of 0.3 g/cc from our QMD simulations that are plotted on the left column of Figs. 6(a)–6(c) (red lines) along with their values for ambient water (black dashed lines). The total pair distribution function, $g(r)$, and neutron weighted pair distribution function, $g_N(r)$, are also plotted in Figs. 6(d) and 6(e), respectively. Computed bond angles of water at 1000 K with density of 1.0 g/cc are plotted in red in the middle column along with the ones computed for water under ambient conditions plotted by the black dashed lines. The double covalent H–O–H bond angle is shown in Fig. 6(f). Figure 6(g) shows the H–O–H bond angle between the H–O hydrogen bond and the O–H covalent bond. The single dash indicates covalent bond, and two dashes indicate the hydrogen bond. Figure 6(h) shows the double hydrogen bond angle H–O–H. Figure 6(i) shows the O–H–O bond angle between the covalent O–H bond and the hydrogen H–O bond and the middle column of Fig. 6(j) shows the intermolecular OOO bond angle. Computed partial structure factors $S_{\alpha\beta}(q)$ are plotted on the right columns of Figs. 6(k)–6(m) (in red) along with the computed partials plotted by the black dashed lines. The x-ray structure factor, $S_X(q)$, and the neutron structure factor, $S_N(q)$, are also plotted in Figs. 6(n) and 6(o), respectively.

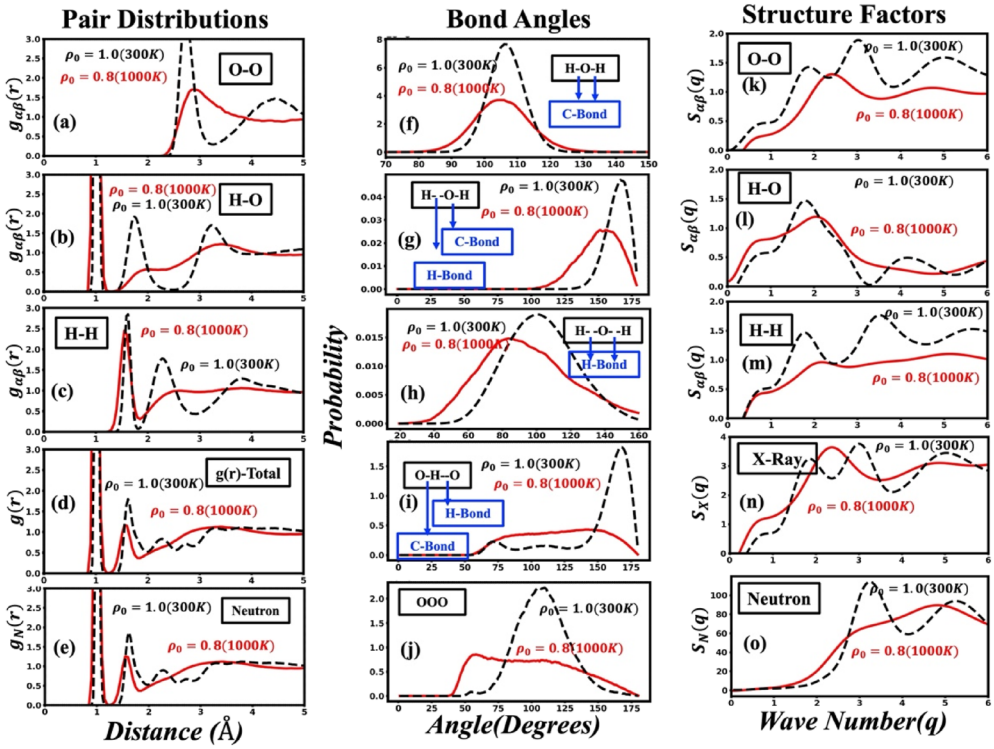

FIG. 4. Calculated structural properties of water at 1000 K, with a density of 0.8 g/cc from our QMD simulations are plotted by the red lines. The structural properties of water at ambient temperature and pressure (300 K, 1.0 g/cc) are also plotted by the black dashed lines. The columns from left to right represent calculated pair distribution functions, bond angles, and various structure factors, respectively.

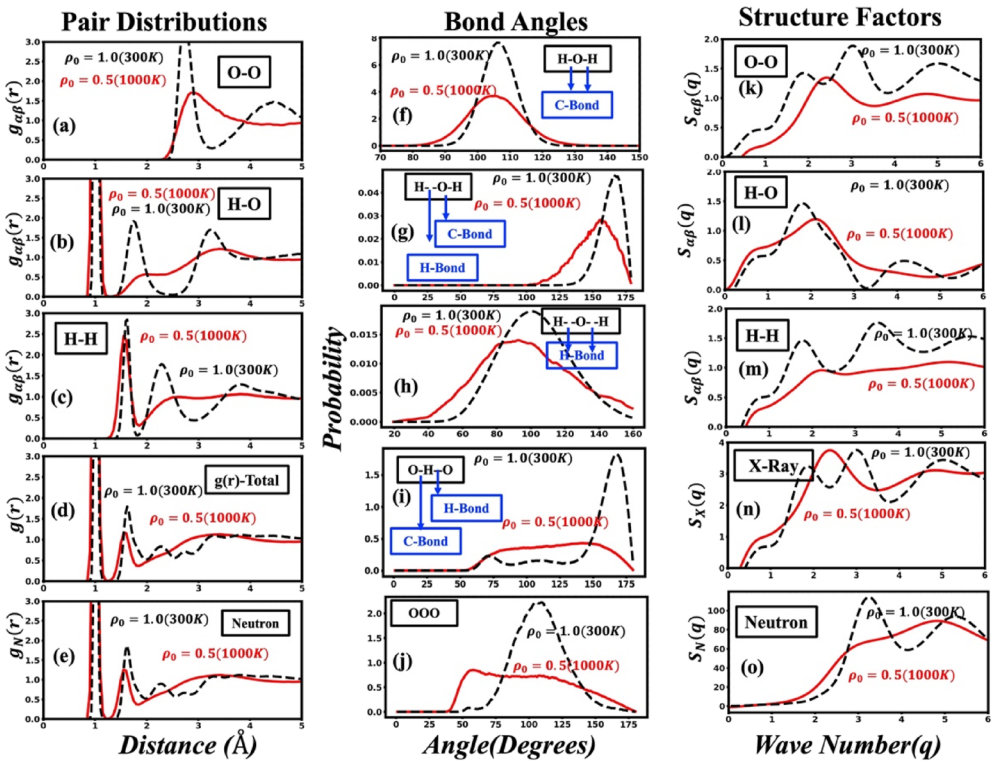

FIG. 5. Calculated structural properties of water at 1000 K, with a density of 0.5 g/cc from our QMD simulations are plotted by the red lines). The structural properties of water at ambient temperature and pressure (300 K, 1.0 g/cc) are plotted by the black dashed lines. The columns from left to right represent calculated pair distribution functions, bond angles, and various structure factors, respectively.

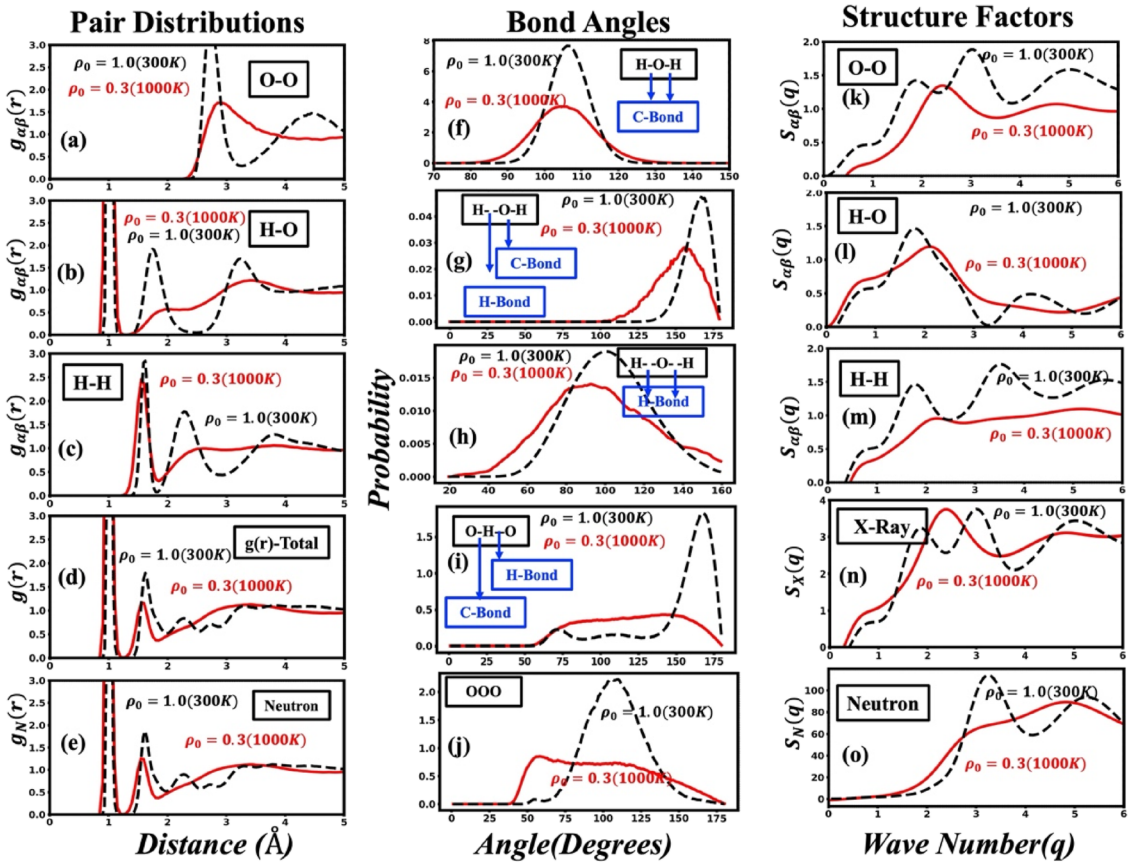

FIG. 6. Calculated structural properties of water at 1000 K, with a density of 0.3 g/cc from our QMD simulations are plotted by the red line). The structural properties of water at ambient temperature and pressure (300 K, 1.0 g/cc) are plotted by the black dashed lines. The columns from left to right represent calculated pair distribution functions, bond angles, and various structure factors, respectively.

Structural correlations along with partial pair distribution functions, $g_{\alpha\beta}(r)$, at a density of 0.1 g/cc from QMD trajectories are plotted in the left columns of Figs. 7(a)–7(c) (red) along with their values for ambient water (black dashed lines). The total pair distribution function, $g(r)$, and neutron weighted pair distribution function, $g_N(r)$, are also plotted in Figs. 7(d) and 7(e), respectively. Computed bond angles of water at 1000 K with density of 1.0 g/cc are plotted by the red lines in the middle column along with the ones computed for water under ambient conditions plotted by the black dashed lines. The double covalent H–O–H bond angle is shown in Fig. 7(f). Figure 7(g) shows the H–O–H bond angle between the H–O hydrogen bond and the O–H covalent bond. The single dash indicates covalent bond, and two dashes indicate the hydrogen bond. Figure 7(h) shows the double hydrogen bond angle H–O–H. Figure 7(i) shows the O–H–O bond angle between the covalent O–H bond and the hydrogen H–O bond and the middle column of Fig. 7(j) shows the intermolecular OOO bond angle. Computed partial structure factors $S_{\alpha\beta}(q)$ are plotted in the right columns of Figs. 7(k)–7(m) (in red) along with the computed partials plotted by the black dashed lines. The x-ray structure factor $S_X(q)$ and the neutron structure factor $S_N(q)$ are also plotted in Figs. 7(n) and 7(o), respectively.

We conclude this section by examining the nature of the hydrogen bond network in supercritical water based on partial pair distribution functions, $g_{\mathrm{HO}}(r)$ and $g_{\mathrm{OO}}(r)$, and bond angle distribution for the covalent H–O–H bond within the molecule and distribution of bond angles that show the angle between covalent and hydrogen bonds, H–O–H, and hydrogen bond–hydrogen bond angle, H–O–H.

We first examine the integrity of water molecules at the lowest density of our simulations at 0.1 g/cc, by looking the intra-molecular H–O correlations given in Fig. 7(b) and H–H correlations shown in Fig. 7(c) and the nature of molecular disorder by examining O–O correlations between water molecules given in Fig. 12(a). From the first peak in $g_{\mathrm{HO}}(r)$ shown in Fig. 7(b), it is clear that the O–H covalent bond is intact at 0.98 Å and from the first peak in $g_{\mathrm{HH}}(r)$ shown in Fig. 7(c), it is given that intramolecular H–H distance is robust at 1.68 Å. These two observations confirm that the water molecule, even though thermally agitated, is quite robust at 1000 K at a density of 0.1 g/cc. It is well known that water's pH value changes as a result

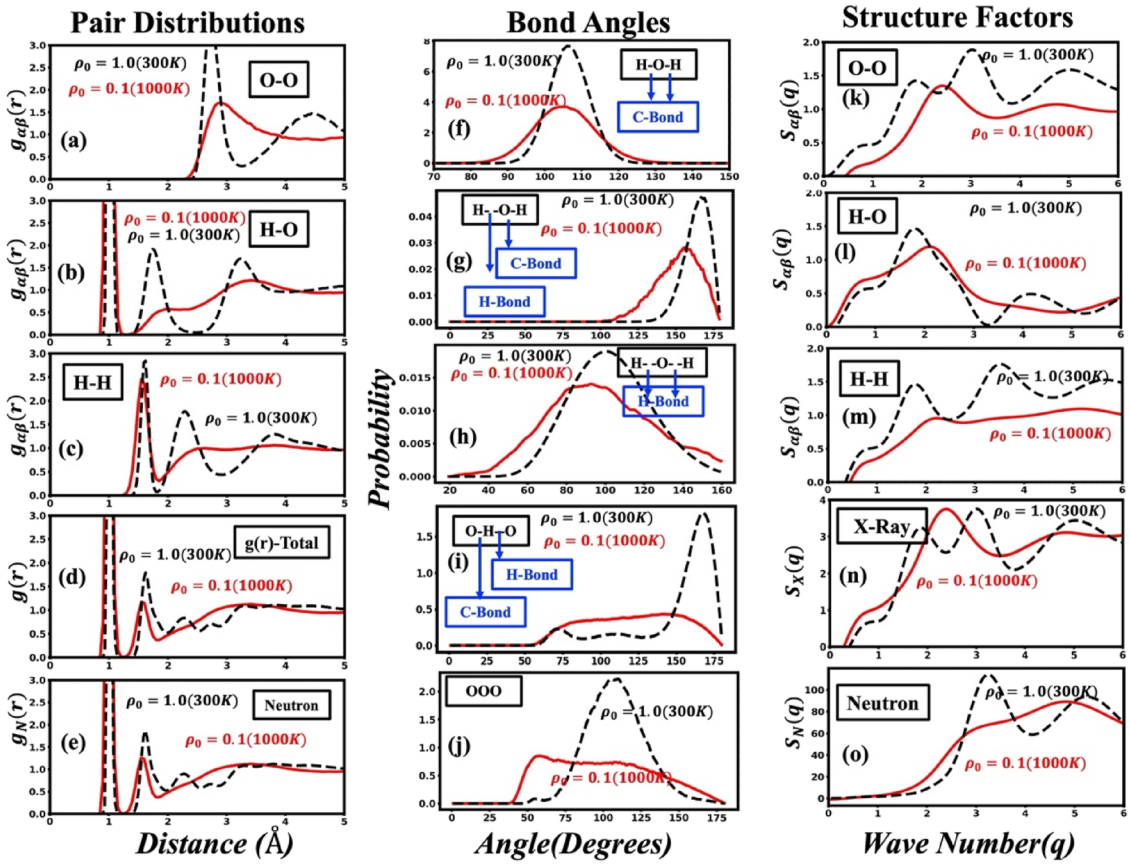

FIG. 7. Calculated structural properties of water at 1000 K, with a density of 0.1 g/cc from our QMD simulations (plotted in red). The structural properties of water at ambient temperature and pressure (300 K, 1.0 g/cc) are plotted by the black dashed lines. The columns from left to right represent calculated pair distribution functions, bond angles, and various structure factors, respectively.

of breaking of water molecules at high temperatures. However, in our QMD sample of 108 molecules, such events are not present simply due to the fact that a negligibly small fraction of water molecule breaks, producing H and OH ions. From the second peak in $g_{\mathrm{HO}}(r)$ shown in Fig. 7(b), it is clear that the well-defined hydrogen bond peak at 1.73 Å in ambient water is broadened greatly and combined with the third peak. Only a small shoulder is left at 1.987 Å of the hydrogen bond peak, which is a result of large excursions of the O–H hydrogen bond that is overlapping with the third peak, which is not due to hydrogen bonding.

Let us now discuss the nature of the hydrogen bond as characterized by bond angle distributions. We first examine the H–O–H bond angle distribution that defines the internal angle within the water molecule, as shown in Fig. 7(f). The distribution has a clear peak at 102° that is a bit asymmetric toward lower angles instead of a symmetric peak at 104° in ambient water. This confirms that the water molecule, although thermally agitated, is quite robust at 1000 K at 0.1 gr/cc. We now examine the H–O–H bond angle, the angle between hydrogen bond with the covalent bond within water molecule shown in Fig. 7(g). This bond angle is clearly defined at 165° in ambient water, and at 0.1 g/cc, the peak broadens toward lower angles with the peak at 150°. However, the peak is clearly well-defined. The angle between two hydrogen bonds, H–O–H bond angle, is shown in Fig. 7(h). This distribution is considerably broadened with a shift in the peak at a lower angle of 90°. This broad distribution is a result of low density and great thermal agitation in the system. However, we can clearly conclude that the hydrogen bond network at a density of 0.1 g/cc at 1000 K is very agitated with considerable distortion, as manifested in broader bond-angle distributions H–O–H shown in Fig. 7(h). However, the H–O–H distribution has an identifiable peak, although covering much broader angles from 40° to 160°. Clearly, this highly agitated and distorted H-bond network will result in a much shorter lifetime of the hydrogen bond at 0.1 g/cc at 1000 K when compared to the lifetime in ambient water.

In summary, comparing the effects of temperature and density reveals a clear hierarchy in how water responds to extreme conditions. Changes in density at 1000 K, even as large as reducing it by an order of magnitude from 1.0 to 0.1 g/cc, result in broadened and weakened hydrogen bond network, while leaving the basic integrity

of water molecule almost fully intact. The O–O, H–O, and H–H correlations all preserve their fundamental intramolecular signatures, and the characteristic angle distributions, although broadened, still retain identifiable peaks that reflect a coherent but highly agitated network. The structural plots at lower densities are very similar to the system with a density of 1.0 g/cc at 1000 K. Although lowering the density introduces disorder through larger molecular excursions and a more diffuse hydrogen bond environment, it is the rise in temperature that truly dismantles the extended structure hydrogen network in water. Temperature, not density, is, therefore, the dominant driver of degradation of the hydrogen network, erasing the long-range connectivity of the hydrogen bond network even as the individual water molecule itself remains remarkably resilient.

In a later publication, we will discuss the unique characterization of a hydrogen bond in supercritical water based on the charge density overlap.

IV. DYNAMICAL CORRELATIONS AND VALIDATION WITH EXPERIMENT ON SCW AT 0.625 g/cc AT 625 K

A. Dynamical correlations and validation of vibrational density-of-states with neutron scattering experiment

We next study vibrational correlations by computing velocity and current autocorrelation functions. The velocity autocorrelation function is defined as $F(t) = \frac{\langle v_i(t).v_i(0)\rangle}{\langle v_i(0).v_i(0)\rangle}$, where $v_i(t)$ is the velocity of the ith atom at time t and the $\langle\rangle$ brackets denote the averages over ensembles and atoms. The current–current correlation function is defined as $G(t) = \frac{\langle J(t).J(0)\rangle}{\langle J(0).J(0)\rangle}$, where the charge current is given by $J(t) = \sum_i z_i \vec{v_i}(t)$, with z_i being the charge of the ith ion.

The vibrational density of states is obtained by the Fourier transform of the corresponding velocity autocorrelation function,[38]

$$F_\alpha(\omega) = \frac{6N_\alpha}{\pi} \int_0^\infty F_\alpha(t)\cos(\omega t)dt. \tag{5}$$

The frequency-dependent ionic conductivity can be calculated from the Fourier transform of the current–current correlation function,

$$G(\omega) = \frac{2\langle J(0)^2\rangle}{3Vk_BT} \int_0^\infty G(t)\cos(\omega t)dt, \tag{6}$$

where V is the volume of the system and k_B is the Boltzmann constant.

Let us first consider the vibrational spectra of water, H_2O. The H_2O molecule exhibits three main experimentally observed frequencies.

1. O–H symmetric stretch at 453.4 meV (3657 cm^{-1}).[43]
2. O–H asymmetric stretch at 465 meV (3756 cm^{-1}).[43]
3. H–O–H bending at 197.7 meV (1595 cm^{-1}).[43]

These frequencies manifest as bands in liquid water, illustrated in Fig. 8, which also shows the atomically resolved vibrational density of states $F_H(\omega)$ and $F_O(\omega)$ of the total $F(\omega)$. The lower part of Fig. 8 presents the Fourier transform of the current–current auto-correlation function.

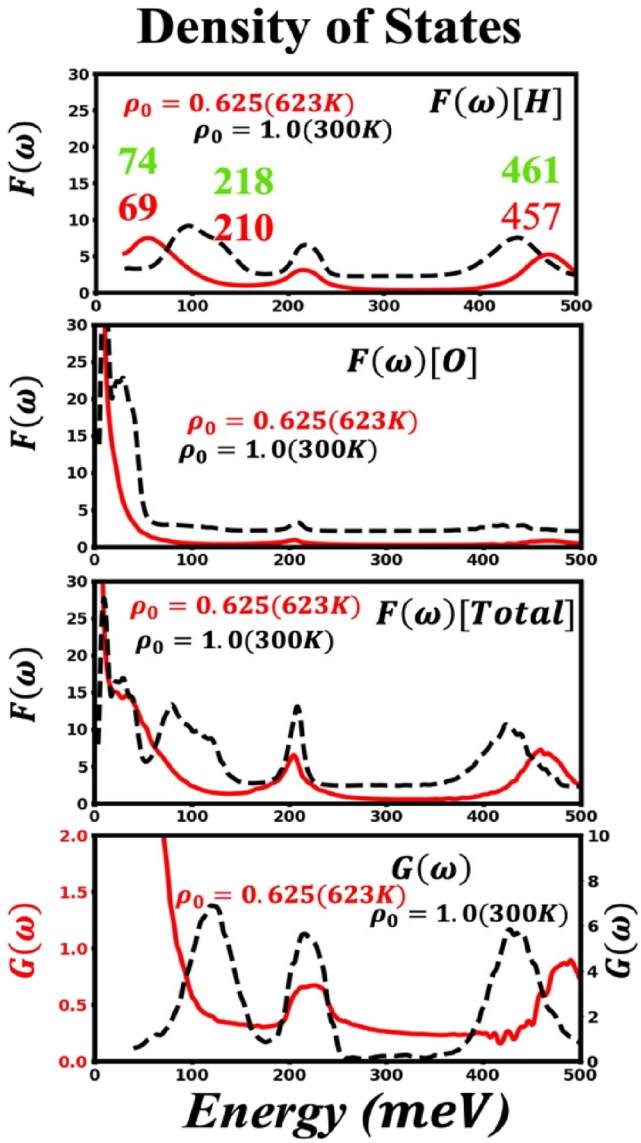

FIG. 8. QMD simulation vibrational density of states $F(\omega)$ and Fourier transform of the current–current correlation $G(\omega)$ for water at 300 K at density 1.0 g/cc (black dotted line) and supercritical water at 623 K at density of 0.625 g/cc (red solid line). The experimental peak positions of the hydrogen projected vibrational density of states for the supercritical water system (0.625 g/cc at 623 K) are given in the figure in green color. The experimental values were taken from the neutron scattering study by Andreani *et al.*[44] [Reproduced with permission from Andreani *et al.*, J. Phys. Chem. Lett. **11**(21), 9461–9467 (2020). Copyright 2020 American Chemical Society] in green color, with the corresponding calculated values from our simulations given in red color.

While the vibrational density-of-states displays all vibrational modes, independent of any selection rules, $G(\omega)$ only highlights dipole-active modes. Since the three intramolecular modes of water are dipole-active, comparing them directly with $G(\omega)$ in liquid water is highly valuable. In our QMD simulations of liquid

water, we observe these O–H symmetric and asymmetric peaks at 406.6 and 424.6 meV, respectively, and the H–O–H peak at 203 meV, which closely align with the molecular frequencies of isolated H_2O molecules. Frequencies in our simulations concur for the OH bending and stretching features at ~200 and 450 meV, respectively.[45–50]

Beyond these intramolecular vibrations, liquid water also exhibits modes arising from O–O interactions between molecules, small water clusters, and various rotational–translational modes, which occur in the low-frequency range below 150 meV. The peak at around ~30 meV is attributed to the frequency of hydrogen bond stretches,[50] while the reorientation of water molecules is associated with the peak at 94 meV.[50]

It is important to note that discrepancies between our simulations and experimental results are primarily due to the pseudopotential approximation and the choice of SCAN exchange–correlation function used in DFT calculations. To the best of our knowledge, no exchange–correlation function perfectly reproduces experimental frequencies in liquid water. While structural correlations are determined by the location of potential energy minima, frequencies are determined by the curvature of the potential energy function at the minima. Therefore, deviations between experimental and simulation values for vibrational modes in liquids are more significant compared to structural values. Nevertheless, these deviations can serve as a tool to refine exchange–correlation functions used in DFT calculations for water and related systems.

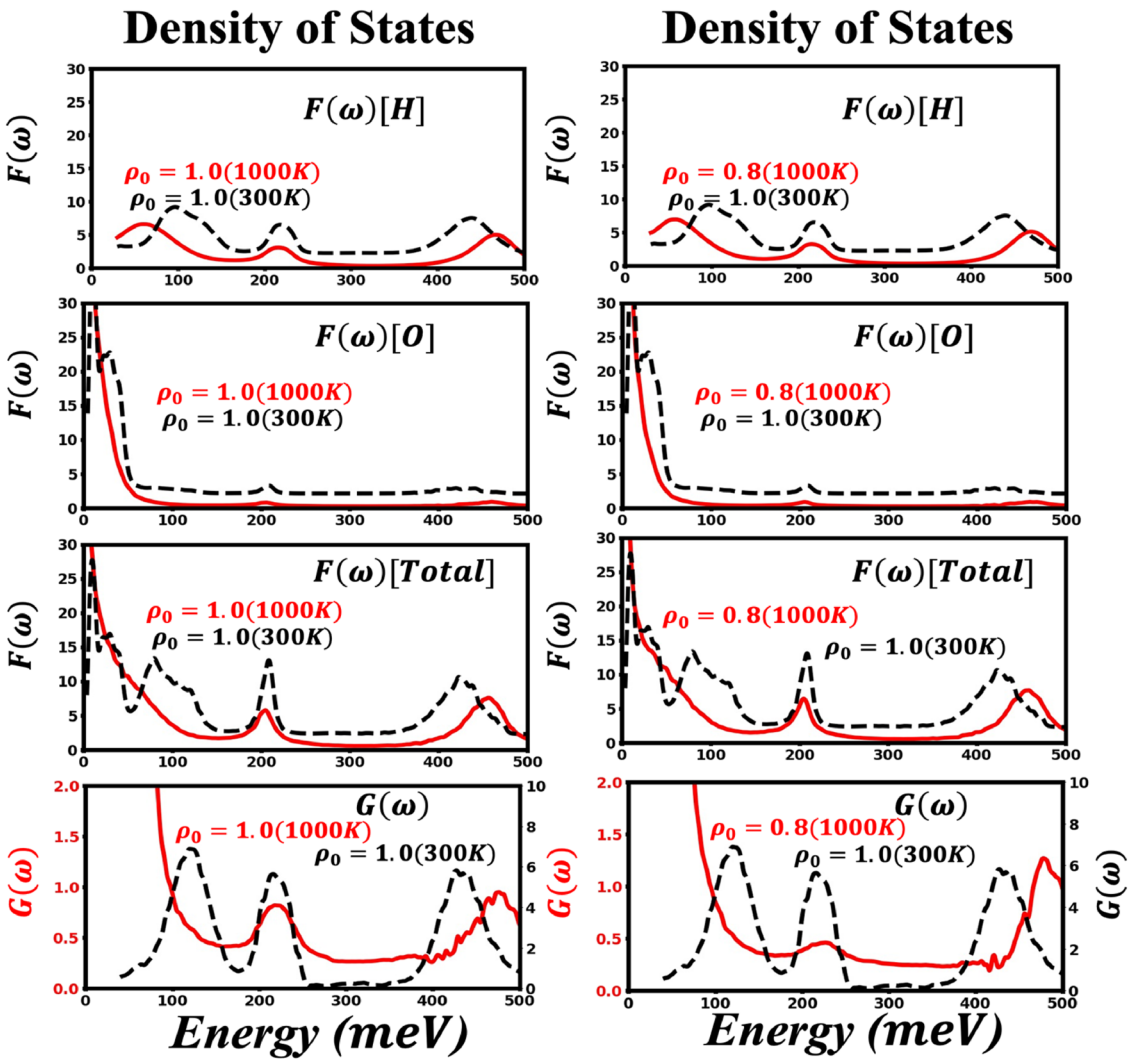

FIG. 9. QMD calculated vibrational density of states $F(\omega)$ and Fourier transform of the current–current correlation $G(\omega)$ for water at 300 K with density of 1.0 g/cc (black dotted line) and supercritical water at 1000 K with density of 1.0 g/cc (left column) and 0.8 g/cc (right column) (both in solid red line).

We have also calculated the vibrational density of states (VDoS) by Fourier transforming the velocity autocorrelation function for supercritical water. The validation for the VDoS from our simulations is carried out by comparing our results with the inelastic neutron scattering experiments on SCW water at a density of 0.75 g/cc at 673 K by Andreani *et al.*[44] This validation and detailed results for dynamical correlations on SCW at ten densities will be presented in Sec. IV B.

B. Dynamical correlation: Results for vibrational density of states and frequency-dependent dielectric function for supercritical water

Here, we present our analysis of the vibrational properties of supercritical water at 1000 K. The results for densities of 1.0, 0.8, 0.5, 0.3, and 0.1 g/cc are discussed in this section, while plots corresponding to intermediate densities of 0.9, 0.7, 0.6, 0.4, and 0.2 g/cc are provided in the supplementary material.

The changes observed in the calculated vibrational density of states (VDoS) from 300 to 1000 K shown in Fig. 9 closely match the corresponding changes in the experimental spectra, as shown in Fig. 8. Notably, both datasets show a blue shift[44] in the stretching frequency, while the bending frequency remains largely unchanged. Figures 10 and 11 show the vibrational density of states $F(\omega)$ and the Fourier transform of the current-current correlation $G(\omega)$ for ambient water and supercritical water from QMD simulation

This is even more evident when we put the VDoS on the same plot as a function of density shown in Fig. 12.

Table I presents data on the relationship between density and the O–H stretch peak position (measured in meV).

For ambient water at a density of 1.0 g/cc, the peak position is 424.6 meV. However, for water at 1000 K with a density of 1.0 g/cc,

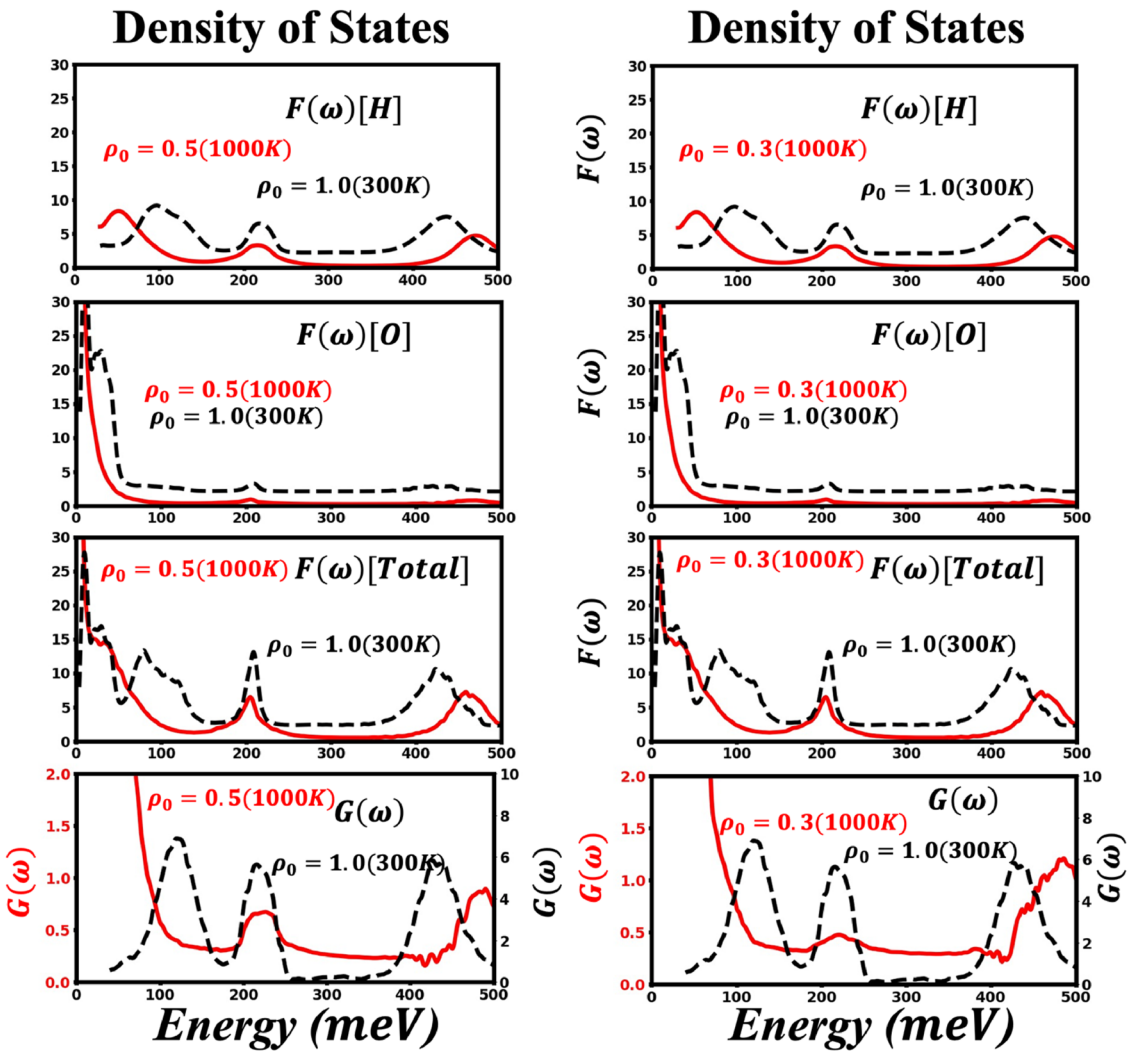

FIG. 10. QMD calculated vibrational density of states $F(\omega)$ and Fourier transform of the current–current correlation $G(\omega)$ for water at 300 K with density 1.0 g/cc (black dotted line) and supercritical water at 1000 K with density of 0.5 g/cc (left column) and 0.3 g/cc (right column) (both in solid red line).

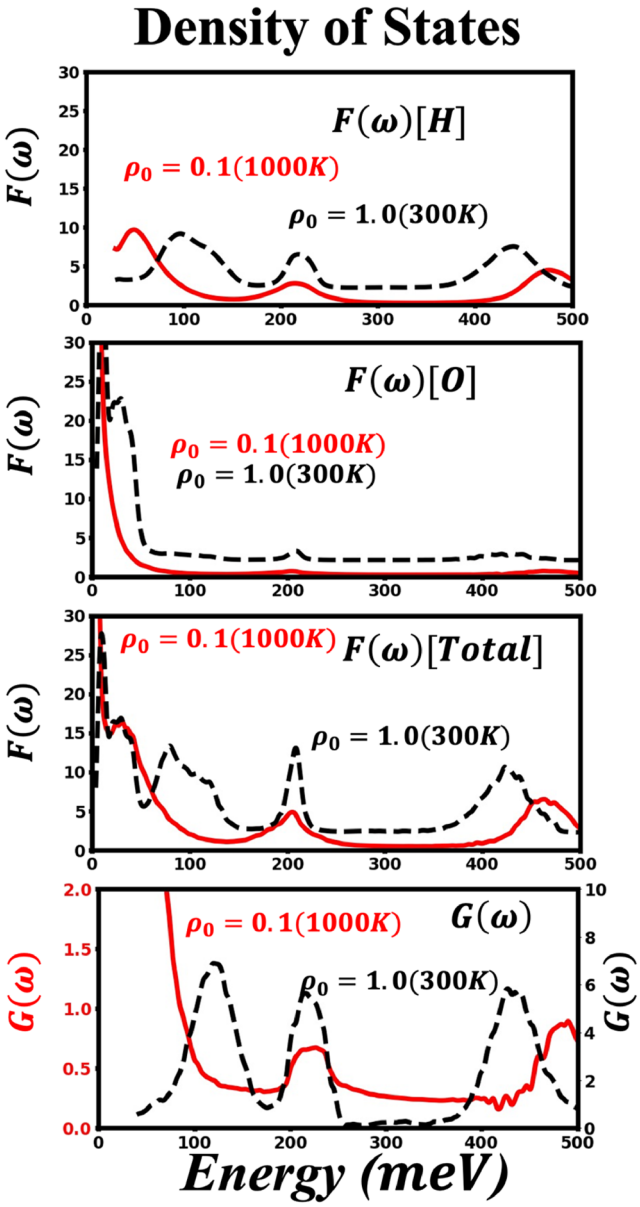

FIG. 11. QMD calculated vibrational density of states $F(\omega)$ and Fourier transform of the current–current correlation $G(\omega)$ for water at 300 K with density 1.0 g/cc (black dotted line) and supercritical water at 1000 K with density of 0.1 g/cc (in solid red line).

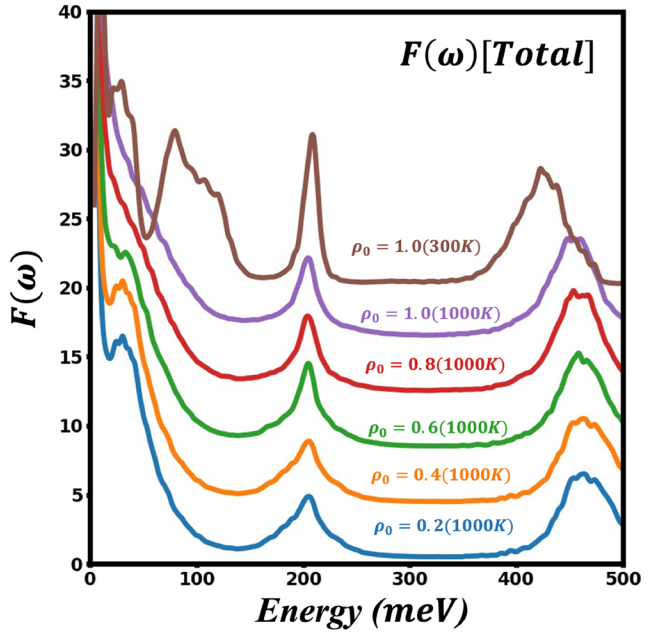

FIG. 12. Blue shift in the stretching frequency >450 meV is clearly observed as the density of supercritical water decreases. The energy values at the peak are given in Table I.

TABLE I. Energy of the O–H stretching mode peak positions for various densities of supercritical water at 1000 K. The value at 300 K is given for reference in the first row.

Density (g/cc)	Peak position (meV)
1.0 (300 K)	424.6
1.0 (1000 K)	451.2
0.8 (1000 K)	457.1
0.6 (1000 K)	459.09
0.4 (1000 K)	461.01
0.2 (1000 K)	461.2

the peak position is 451.2 meV. As the density decreases, the peak position shifts upward, reaching 461.2 meV at a density of 0.2 g/cc.

Taken together, the structural correlations and vibrational spectra presented in this work reveal a consistent and unifying picture of how temperature and density affect the behavior of supercritical water. The O–H stretching peak energy increases from 424.6 meV at 300 K to 451.2 meV at 1000 K at a fixed density of 1.0 g/cc, a shift far larger than the additional increase to 461 meV from 451.2 meV observed when density is reduced by nearly an order of magnitude. This trend mirrors the structural analysis: temperature strongly disrupts the extended hydrogen–bond network, shifts the O–O coordination shell outward, and erases intermediate-range order, while the molecular integrity of the remains remarkably intact. Density variations at 1000 K, by contrast, primarily tune the extent of intermolecular electronic perturbation on the covalent O–H bond. At higher density, strong hydrogen bonding and partial electronic delocalization soften the O–H stretch, whereas at lower density, the reduced intermolecular coupling localizes the O–H bond and steepens it, producing the gradual blue shift. These findings show that although density modulates the degree of intermolecular influence, it is temperature that plays the dominant role in altering the structure and dynamics of water under extreme conditions. The combined evidence establishes that supercritical water transitions from a structured, hydrogen-bonded liquid to a

highly disordered, weakly correlated fluid primarily through thermal effects, with density acting as a secondary but coherent modifier of its vibrational and structural response.

V. CONCLUSION

To conclude, in this study, we examined the partial pair distribution functions and bond angle distributions of water with densities ranging from 1 to 0.1 g/cc at 1000 K. In addition to these structural correlations, we also calculated the vibrational density of states and current–current correlations in these systems. Our findings confirm that despite extreme thermal agitation, the covalent O–H bond within the water molecule remains intact, as seen in pair distribution functions. The intramolecular H–H distance is also preserved. Robustness of the O–H covalent bond is reflected in the blue shifting of the O–H stretching peaks in the VDoS. However, the hydrogen bond network undergoes a great deal of distortion, and at the lowest density of 0.1 g/cc, it is very agitated, leading to very broad H–O–H distribution and a hard to define H-bond network. Our conclusions about the H-bond network in SCW are in agreement with the experimental findings of Andreani *et al.*[44] who concluded that the breakdown of the percolating H-bond network in water at 733 K is characterized by fleeting and weak intermolecular H-bonds and stiff covalent intramolecular bonds.

SUPPLEMENTARY MATERIAL

We have provided the structural and vibrational correlation results for densities of 0.9, 0.7, 0.6, 0.4, and 0.2 in the supplementary material.

ACKNOWLEDGMENTS

This research was supported by the U.S. Department of Energy, Office of Basic Energy Sciences, Division of Materials Sciences and Engineering, Neutron Scattering and Instrumentation Sciences program under Award No. DE-SC0023146.

AUTHOR DECLARATIONS

Conflict of Interest

The authors have no conflicts to disclose.

Author Contributions

Nitish Baradwaj: Data curation (equal); Formal analysis (equal); Investigation (equal); Methodology (equal); Software (equal); Validation (equal); Visualization (equal); Writing – original draft (equal); Writing – review & editing (equal). **Ken-ichi Nomura**: Conceptualization (supporting); Funding acquisition (supporting); Resources (supporting); Writing – review & editing (supporting). **Aiichiro Nakano**: Funding acquisition (supporting); Supervision (supporting); Writing – review & editing (supporting). **Rajiv K. Kalia**: Funding acquisition (supporting); Supervision (supporting); Writing – review & editing (supporting). **Priya Vashishta**: Conceptualization (equal); Funding acquisition (lead); Project administration (lead); Supervision (lead); Writing – review & editing (equal).

DATA AVAILABILITY

The data that support the findings of this study are available from the corresponding author upon reasonable request.

REFERENCES

[1] P. H. Gleick, and Pacific Institute for Studies in Development, Environment, and Security, Stockholm Environment Institute, *Water in Crisis* (Oxford University Press., 1993), Vol. 9, pp. 1051–0761.
[2] M. Hirschmann and D. Kohlstedt, "Water in Earth's mantle," Phys. Today **65**(3), 40–45 (2012).
[3] J. Korenaga, N. J. Planavsky, and D. A. D. Evans, "Global water cycle and the coevolution of the Earth's interior and surface environment," Philos. Trans. R. Soc., A **375**, 20150393 (2017).
[4] H. Weingärtner and E. U. Franck, "Supercritical water as a solvent," Angew. Chem., Int. Ed. **44**, 2672–2692 (2005).
[5] E. Boulard *et al.*, "New host for carbon in the deep Earth," Proc. Natl. Acad. Sci. U. S. A. **108**, 5184–5187 (2011).
[6] M. Hovland, H. G. Rueslåtten, H. K. Johnsen, B. Kvamme, and T. Kuznetsova, "Salt formation associated with sub-surface boiling and supercritical water," Mar. Pet. Geol. **23**, 855–869 (2006).
[7] M. Hovland, H. Rueslåtten, and H. K. Johnsen, "Buried hydrothermal systems: The potential role of supercritical water, 'ScriW,' in various geological processes and occurrences in the sub-surface," Am. J. Anal. Chem. **05**, 128–139 (2014).
[8] J. W. Tester *et al.*, "Supercritical water oxidation technology: Process development and fundamental research," ACS Symp. Ser. **518**, 35 (1993).
[9] Y. Marcus, *Supercritical Water: A Green Solvent: Properties and Uses* (John Wiley & Sons, 2012).
[10] M. D. Bermejo and M. J. Cocero, "Supercritical water oxidation: A technical review," AIChE J. **52**, 3933–3951 (2006).
[11] P. Kritzer and E. Dinjus, "An assessment of supercritical water oxidation (SCWO): Existing problems, possible solutions and new reactor concepts," Chem. Eng. J. **83**, 207–214 (2001).
[12] P. A. Marrone, S. D. Cantwell, and D. W. Dalton, "SCWO system designs for waste treatment: Application to chemical weapons destruction," Ind. Eng. Chem. Res. **44**, 9030–9039 (2005).
[13] C. J. Sahle *et al.*, "Microscopic structure of water at elevated pressures and temperatures," Proc. Natl. Acad. Sci. U. S. A. **110**, 6301–6306 (2013).
[14] Q. Sun, Q. Wang, and D. Ding, "Hydrogen bonded networks in supercritical water," J. Phys. Chem. B **118**, 11253–11258 (2014).
[15] P. Wernet *et al.*, "Spectroscopic characterization of microscopic hydrogen-bonding disparities in supercritical water," J. Chem. Phys. **123**, 154503 (2005).
[16] A. Chialvo and P. Cummings, in *Supercritical Fluids: Fundamentals and Applications* (Springer, 2000), pp. 345–394.
[17] A. K. Soper, "The radial distribution functions of water and ice from 220 to 673 K and at pressures up to 400 MPa," Chem. Phys. **258**, 121–137 (2000).
[18] T. Head-Gordon and M. E. Johnson, "Tetrahedral structure or chains for liquid water," Proc. Natl. Acad. Sci. U. S. A. **103**, 7973–7977 (2006).
[19] P. Postorino, R. H. Tromp, M.-A. Ricci, A. K. Soper, and G. W. Neilson, "The interatomic structure of water at supercritical temperatures," Nature **366**, 668–670 (1993).
[20] J. D. Frantz, J. Dubessy, and B. Mysen, "An optical cell for Raman spectroscopic studies of supercritical fluids and its application to the study of water to 500 °C and 2000 bar," Chem. Geol. **106**, 9–26 (1993).
[21] T. Tassaing, P. A. Garrain, D. Bégué, and I. Baraille, "On the cluster composition of supercritical water combining molecular modeling and vibrational spectroscopic data," J. Chem. Phys. **133**, 034103 (2010).

[22]C. Schmidt and A. Watenphul, "Ammonium in aqueous fluids to 600 °C, 1.3GPa: A spectroscopic study on the effects on fluid properties, silica solubility, and K-feldspar to muscovite reactions," Geochim. Cosmochim. Acta **74**, 6852–6866 (2010).
[23]M. M. Hoffmann and M. S. Conradi, "Are there hydrogen bonds in supercritical water?," J. Am. Chem. Soc. **119**, 3811–3817 (1997).
[24]G. N. I. Clark, G. L. Hura, J. Teixeira, A. K. Soper, and T. Head-Gordon, "Small-angle scattering and the structure of ambient liquid water," Proc. Natl. Acad. Sci. U. S. A. **107**, 14003–14007 (2010).
[25]F. Sedlmeier, D. Horinek, and R. R. Netz, "Spatial correlations of density and structural fluctuations in liquid water: A comparative simulation study," J. Am. Chem. Soc. **133**, 1391–1398 (2011).
[26]D. Prendergast and G. Galli, "X-ray absorption spectra of water from first principles calculations," Phys. Rev. Lett. **96**, 215502 (2006).
[27]W. Chen, X. Wu, and R. Car, "X-ray absorption signatures of the molecular environment in water and ice," Phys. Rev. Lett. **105**, 017802 (2010).
[28]J. P. Perdew and K. Schmidt, AIP Conf. Proc. **577**(1), 1–20 (2001).
[29]D. M. Ceperley and B. J. Alder, "Ground state of the electron gas by a stochastic method," Phys. Rev. Lett. **45**, 566–569 (1980).
[30]C. Lee, W. Yang, and R. G. Parr, "Development of the Colle-Salvetti correlation-energy formula into a functional of the electron density," Phys. Rev. B **37**, 785 (1988).
[31]R. Car, "Fixing Jacob's ladder," Nat. Chem. **8**, 820–821 (2016).
[32]J. Sun *et al.*, "Accurate first-principles structures and energies of diversely bonded systems from an efficient density functional," Nat. Chem. **8**, 831–836 (2016).
[33]G. Kresse and J. Furthmuller, "Efficient iterative schemes for ab initio total-energy calculations using a plane-wave basis set," Phys. Rev. B **54**, 11169–11186 (1996).
[34]M. C. Payne, M. P. Teter, D. C. Allan, T. A. Arias, and J. D. Joannopoulos, "Iterative minimization techniques for *ab initio* total-energy calculations: Molecular dynamics and conjugate gradients," Rev. Mod. Phys. **64**, 1045–1097 (1992).
[35]P. E. Blöchl, "Projector augmented-wave method," Phys. Rev. B **50**, 17953–17979 (1994).
[36]P. Hohenberg and W. Kohn, "Inhomogeneous electron gas," Phys. Rev. **136**, B864–B871 (1964).
[37]J. Sun, A. Ruzsinszky, and J. P. Perdew, "Strongly constrained and appropriately normed semilocal density functional," Phys. Rev. Lett. **115**, 036402 (2015).
[38]A. Krishnamoorthy *et al.*, "Dielectric constant of liquid water determined with neural network quantum molecular dynamics," Phys. Rev. Lett. **126**, 216403 (2021).
[39]P. Vashishta, R. K. Kalia, J. P. Rino, and I. Ebbsjö, "Interaction potential for SiO_2—A molecular-dynamics study of structural correlations," Phys. Rev. B **41**, 12197–12209 (1990).
[40]M. Bernabei, A. Botti, F. Bruni, M. A. Ricci, and A. K. Soper, "Percolation and three-dimensional structure of supercritical water," Phys. Rev. E **78**, 021505 (2008).
[41]A. K. Soper, F. Bruni, and M. A. Ricci, "Site–site pair correlation functions of water from 25 to 400 °C: Revised analysis of new and old diffraction data," J. Chem. Phys. **106**, 247–254 (1997).
[42]A. K. Soper, "The radial distribution functions of water as derived from radiation total scattering experiments: Is there anything we can say for sure?," Int. Scholarly Res. Not. **2013**, 1–67.
[43]K. Nakamoto, *Infrared and Raman Spectra of Inorganic and Coordination Compounds, Part B: Applications in Coordination, Organometallic, and Bioinorganic Chemistry* (John Wiley & Sons, 2009).
[44]C. Andreani *et al.*, "Hydrogen dynamics in supercritical water probed by neutron scattering and computer simulations," J. Phys. Chem. Lett. **11**, 9461–9467 (2020).
[45]G. S. Fanourgakis and S. S. Xantheas, "Development of transferable interaction potentials for water. V. Extension of the flexible, polarizable, Thole-type model potential (TTM3-F, v. 3.0) to describe the vibrational spectra of water clusters and liquid water," J. Chem. Phys. **128**, 074506 (2008).
[46]C. J. Burnham, D. J. Anick, P. K. Mankoo, and G. F. Reiter, "The vibrational proton potential in bulk liquid water and ice," J. Chem. Phys. **128**, 154519 (2008).
[47]P. K. Mankoo and T. Keyes, "POLIR: Polarizable, flexible, transferable water potential optimized for IR spectroscopy," J. Chem. Phys. **129**, 034504 (2008).
[48]T. Ishiyama and A. Morita, "Analysis of anisotropic local field in sum frequency generation spectroscopy with the charge response kernel water model," J. Chem. Phys. **131**, 244714 (2009).
[49]T. Hasegawa and Y. Tanimura, "A polarizable water model for intramolecular and intermolecular vibrational spectroscopies," J. Phys. Chem. B **115**, 5545–5553 (2011).
[50]J. E. Bertie and Z. Lan, "Infrared intensities of liquids XX: The intensity of the OH stretching band of liquid water revisited, and the best current values of the optical constants of H_2O(l) at 25 °C between 15,000 and 1 cm^{-1}," Appl. Spectrosc. **50**, 1047–1057 (1996).